Interfacial alloying between lead halide perovskite crystals and hybrid glasses

Xuemei Li, Wengang Huang, Andraž Krajnc, Yuwei Yang, Atul Shukla, Jaeho Lee, Mehri Ghasemi, Isaac Martens, Bun Chan, Dominique Appadoo, et al.

Interfacial alloying between lead halide perovskite crystals and hybrid glasses

Xuemei Li[1], Wengang Huang[1], Andraž Krajnc[2], Yuwei Yang[3], Atul Shukla[4], Jaeho Lee[1], Merhi Ghasemi[5], Isaac Martens[6], Bun Chan[7], Dominique Appadoo[8], Peng Chen[9], Xiaoming Weng[5], Julian A. Steele[4,10], Qiang Sun[11,12], Gregor Mali[2], Rijia Lin[1], Nicholas Bedford[3], Vicki Chen[1, 13], Anthony K. Cheetham[14], Luiz H. G. Tizei[15], Sean M. Collins[16], Lianzhou Wang[1, 9] and Jingwei Hou[1,*]

[1]School of Chemical Engineering, The University of Queensland, St Lucia, QLD, 4072 Australia

[2]Department of Inorganic Chemistry and Technology, National Institute of Chemistry, 1001 Ljubljana, Slovenia

[3]School of Chemical Engineering, The University of New South Wales, Kensington, NSW 2052 Australia

[4]School of Mathematics and Physics, The University of Queensland, St Lucia, QLD, 4072 Australia

[5]School of Science, RMIT University, Melbourne, VIC 3000, Australia

[6]European Synchrotron Radiation Facility, 71 Avenue des Martyrs, 38000 Grenoble, France

[7]Graduate School of Engineering, Nagasaki University, Nagasaki 852-8521 Japan

[8]Australian Synchrotron, 800 Blackburn Rd, Clayton, VIC, 3168 Australia

[9]Australian Institute for Bioengineering and Nanotechnology, The University of Queensland, St Lucia, QLD, 4072 Australia

[10]cMACS, Department of Microbial and Molecular Systems, KU Leuven, Celestijnenlaan 200F, 3001 Leuven, Belgium

[11]State Key Laboratory of Oral Diseases, National Clinical Research Center for Oral Diseases, West China Hospital of Stomatology, Sichuan University, Chengdu, Sichuan 610041, China

[12]Sichuan Provincial Engineering Research Center of Oral Biomaterials, Chengdu, Sichuan 610041, China

[13]University of Technology Sydney, 15 Broadway, Ultimo, NSW 2007 Australia

[14]Materials Research Laboratory, University of California, Santa Barbara, CA 93106 USA

[15]Université Paris-Saclay, CNRS, Laboratoire de Physique des Solides, 91405, Orsay, France

[16]School of Chemical and Process Engineering and School of Chemistry, University of Leeds, LS2 9JT, UK

Abstract

The stellar optoelectronic properties of metal halide perovskites provide enormous promise for next-generation optical devices with excellent conversion efficiencies and lower manufacturing costs. However, there is a long-standing ambiguity as to whether the perovskite surface/interface (*e.g.* structure, charge transfer or source of off-target recombination) or bulk properties are the more determining factor in device performance. We fabricated an array of $CsPbI_3$ crystal and hybrid glass composites by sintering and globally visualised the property-performance landscape. Our findings reveal that the interface is the primary determinant of the crystal phases, optoelectronic quality, and stability of $CsPbI_3$. In particular, the presence of a diffusion "alloying" layer is discovered to be critical for passivating surface traps, and beneficially altering the energy landscape of crystal phases. However, high-temperature sintering results in the promotion of a non-stoichiometric perovskite and excess traps at the interface, despite the short-range structure of halide is retained within the alloying layer. By shedding light on functional hetero-interfaces, our research offers the key factors for engineering high-performance perovskite devices.

Introduction

Lead halide perovskites feature exceptional optoelectronic properties such as high light-to-energy conversion, emission colour purity, and photoluminescence quantum yield. These characteristics make them a popular candidate for next-generation semiconducting materials to be used within solar panels, sensors, and light-emitting diodes (LEDs)[1-3]. Great effort has been spent in uncovering the mechanistic aspects that contribute to their exceptional performance and finding the origin of their large absorption coefficients, low exciton binding energies, and long carrier diffusion lengths and lifetimes[4-6]. Although immense effort has been devoted to device development, a practical application of perovskites is still hampered by their low stability in multiple aspects[7,8]. For instance, in addition to being susceptible to light, polar solvents and oxygen, the hybrid perovskite formamidinium lead iodide ($FAPbI_3$), which is popular in solar energy conversion, is susceptible to cation sublimation[9,10]. Although inorganic perovskites like $CsPbI_3$ overcome thermal stability issues, polymorphism remains a key challenge, where the optoelectronically active α-, β- and γ-phases exist exclusively at elevated temperatures (>250 °C), with the inactive δ-phase being thermodynamically favoured at ambient temperatures[6,11].

One common strategy for addressing these challenges associated with pure perovskite compounds is to composite them with secondary components [12,13]. Within this context, organic ligands, polymers, inorganic zeolites and glasses, and recently metal–organic frameworks (MOFs) have all been studied, with each type having its own advantages, and simultaneously disadvantages [14-18]. Understanding the behaviour and function of the interface inside the composites is critical. Such knowledge will further aid in the development of more efficient composite materials and devices: perovskites are typically sandwiched between electron and hole transport layers in LEDs and solar panel systems, and the properties of these interfaces can be critical to device performance[19]. However, studying both positive and negative effects from the interface remains a difficult task since most high-performing composites are not

sufficiently stable to keep their original properties/functions against prolonged exposure to handling and inspection[20,21]. Other composites may lack a distinct chemical and/or physical contrast between two phases, reducing the capacity to extract important interfacial information[22].

MOF hybrid glass perovskite composites offer a unique opportunity to pinpoint the interface. The rich structural, chemical, and physical features, as well as the contrasts across phases, allow for the controlled isolation and investigation of the interfaces in composites and the establishment of property-performance correlation. In particular, these high performing composites are stable for characterisation by electron, synchrotron X-ray, and Terahertz beams and storage under ambient conditions[23]. Herein, we fabricated a series of hybrid glassy perovskite composites *via* sintering, and uncovered the origin of their exceptional performance. The atomic-level chemical and structural profile of the $CsPbI_3$ and hybrid glass composite are mapped using a combination of advanced characterisations, revealing the controllable formation of interdiffusion alloying layer during sintering. The layer stabilises $CsPbI_3$ optoelectronic phases and passivates its trap states. On the other hand, alloying can create non-stoichiometric perovskite regions and quenches photoluminescence after high-temperature sintering, despite the preservation of short-range rigid halide structures in the nanometer-thick alloying layer (Figure 1a).

Results and Discussion

Fabrication of composites

The crystal-glass composites were fabricated with pre-formed a_gZIF-62 (a_g refers to amorphous glass) $[Zn(Im)_{1.95}(bIm)_{0.05}]$ (Im: imidazolate and bIm: benzimidazolate) and mechanochemically produced $CsPbI_3$ powders, with detailed procedures in Supplementary Information. Given the polymorphism nature of $CsPbI_3$, computational chemistry (at the xTB level) was applied to investigate its energy profiles. First, we calculated the energies of pure α (cubic) and δ (orthorhombic) $CsPbI_3$ with periodic boundary conditions, finding that the δ-phase was more stable by 18 kJ mol^{-1} per $CsPbI_3$ unit. This is qualitatively consistent with experimental observations and provides a degree of confidence for the use of xTB for further investigations. We then used several molecular cluster models to evaluate the energetics of surface formation to reveal the energy landscape of the $CsPbI_3$ within composites. Figure 1b shows two of the representative products between a fragment of the $CsPbI_3$ surface and an a_gZIF-62 fragment. They were two of the most stable structures that we identified, with ligand exchange at the interface. The generation of the interfacial α-phase product was more exothermic than that of the δ-phase product. At the xTB level, the reaction energies were -1224 (α) and -1033 (δ) kJ mol^{-1}. The difference was sufficient to overcome the inherent stability of the δ-phase over the α-phase (18 kJ mol^{-1} per $CsPbI_3$ unit, and thus by ~150 kJ mol^{-1} for the surface models with 8 or 9 units). The calculation results indicate the interfacial bond favours the formation of optoelectronically active phases of $CsPbI_3$ within composite.

An array of composites was then fabricated with different a_gZIF-62 and $CsPbI_3$ ratios and sintering temperatures. ZIF-62 glass, instead of ZIF-62 crystal, was implemented to promote the formation of adaptive interfaces within the composites, given its higher enthalpy and lower temperature required to access the viscous flowing state[24]. The composite samples were hereby referred to as ($CsPbI_3$)(a_gZIF-62) (X/Y) (prior to sintering) and $(CsPbI_3)_X(a_gZIF\text{-}62)_Y$ (after sintering), where X and Y are the percentage mass of each component, with X values ranging from 1 to 85. Sintering pure $CsPbI_3$ at temperatures greater than 320 ℃ transformed the non-perovskite δ-phase into an optoelectronically active cubic perovskite α-phase, which returned to an inactive δ-phase during returning to ambient (Figure S1)[6,25]. *Ex-situ* X-ray diffraction (XRD) revealed that the $CsPbI_3$ structures within the composites were highly dependent on its fraction and the sintering temperature (Figure 1c and Figure S2). Prior to sintering, the powder mixtures exhibited poor crystallinity as expected for the mechanochemically synthesised $CsPbI_3$. Following the sintering process, $CsPbI_3$ crystallinity enhanced with several phases emerged on top of two a_gZIF-62 broad peaks (centred near 15 and 35°). Higher sintering temperatures and lower $CsPbI_3$ loading, in general, can better preserve the $CsPbI_3$ perovskite phase. Figure 1d and Figure S3 shows a summary of the relative proportion of active γ-$CsPbI_3$ phase within the composites. After sintering at 350 ℃, $(CsPbI_3)_{0.4}(a_gZIF\text{-}62)_{0.6}$ can achieve nearly complete preservation of the γ-phase, and further increase of the $CsPbI_3$ loading resulted in a mixed active γ- and inactive δ-phases. *In-situ* XRD was used to track the sintering-induced phase changes in ($CsPbI_3$)(a_gZIF-62)(40/60) (Figure S4), showing the emergence of active phase $CsPbI_3$ from 150 ℃, which was substantially lower than the intrinsic phase transition temperature of pure $CsPbI_3$ near equilibrium (320 ℃). Further heating improved the crystallinity and the proportion of perovskite crystal formed. After sintering, the composite showed a smooth and continuous surface morphology, with clear phase contrast under scanning electron microscope (SEM, Figure S5).

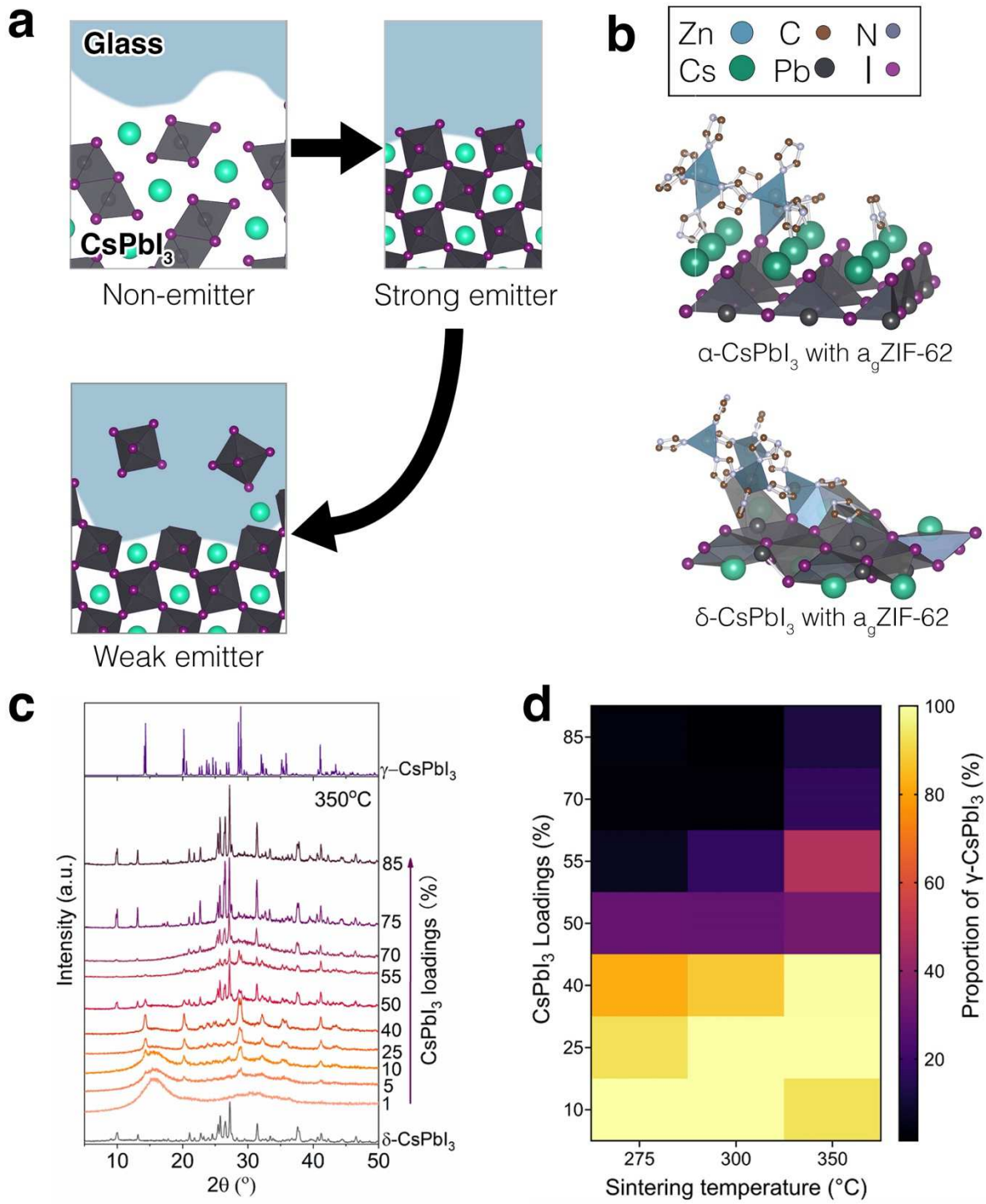

Figure 1. Fabrication of $(CsPbI_3)_X(a_gZIF\text{-}62)_Y$ composites. (a) Schmatic diagram of the $CsPbI_3$ phase transition and evolution of the interfacial atomic structures during sintering. (b) Schematic diagram of the DFT calculation for composites with different $CsPbI_3$ crystal phases. (c) *Ex-situ* XRD pattern of $(CsPbI_3)_X(a_gZIF\text{-}62)_Y$ composites sintered at 350 °C. X-ray λ: 1.5406 Å. (d) γ-phase $CsPbI_3$ proportion within of different $(CsPbI_3)_X(a_gZIF\text{-}62)_Y$ composites, as retrieved from Rietveld refinement of the XRD profiles.

Stable optical performance

The composites exhibited characteristic red-emitting PL under UV excitation, originated from the stable formations of active γ-$CsPbI_3$ phase (Figure S6), with their relative intensity of emissions charted in Figure 2a. The overall PL maximum was realised by $(CsPbI_3)_{0.25}(a_gZIF\text{-}62)_{0.75}$ at 275 °C sintering. The corresponding maximum intensity of the PL emission from composites with different $CsPbI_3$ loadings occurred at different sintering temperatures: generally, samples with greater $CsPbI_3$ loadings achieved their PL maxima at a lower temperature: *e.g.* $(CsPbI_3)_{0.01}(a_gZIF\text{-}62)_{0.99}$ showed a PL maximum for sintering at 300 °C whereas $(CsPbI_3)_{0.85}(a_gZIF\text{-}62)_{0.15}$ showed a PL maximum for sintering at 225 °C. Similar behaviour was also identified for the PL quantum yield (PLQY), with the highest PLQY of 81.3% for $(CsPbI_3)_{0.05}(a_gZIF\text{-}62)_{0.95}$ at 275 °C sintering (Figure S7). This value is greater than the majority of previously reported $CsPbI_3$[26-30]. With increased $CsPbI_3$ loading, the PL peak red-shifted first and then blue-shifted (Figure S8), which was paralleled by similar changes in the γ-phase absorption edge shown in the UV-Vis absorption spectra (Figure S9). The composites demonstrated photostability under continuous excitation, showing negligible shifts in the peak position and variation in intensity during the test (Figure 2b).

Scanning transmission electron microscopy (STEM) based cathodoluminescence (CL) further demonstrated that the $CsPbI_3$ nanometer-scale particles were indeed the source of the light emitted, and the luminescence properties of the composite exhibited different characteristics at the bulk nanocrystals and the interface regions (Figure 2c-f). The emission spectra from these particles peaked at around 710 nm (Figure 2e), and the inter-particle emission peak wavelength varied in the +/-5 nm range based on a Gaussian model fitting of the dataset (Figure S10-11). In the field of view, the variation of the emission intensity was not directly related to the size of the particles, indicating the quantum confinement was not the main contributor to the strong light emission. The width parameter σ of the Gaussian fitted to the emission spectra had a tendency for larger value at the edge of the particles (Figure 2f). Histograms of the fitted coefficients for the data acquired across a relatively large (6.9 μm^2) projected surface showed that the sample was quite homogeneous (Figure S11). In addition, correlations between emission peak center wavelength with its width and intensity were observed (2D histograms in Figure S11). It is worth mentioning that to achieve single particle emission profile STEM lamellae samples were prepared by focused ion beam (FIB), which is known to be prone to damaging perovskites and to quenching CL emission. However, the FIB lamellae emitted light at the same wavelength and with the same emission spectral shape as those powder samples prepared by crushing the composite using a mortar and a pestle, confirming the strong stabilisation effects within the composites.

The PL emission properties from pure perovskites are closely related to their underlying crystal structures and trap states. Enhanced crystallinity should reduce bulk and surface defects, suppressing non-radiative exciton recombination and enhancing PL emission[31,32]. The data presented here, on the other hand, clearly illustrates the presence of additional prominent

effects within the composites, such as the fact that a higher sintering temperature (*e.g.*, >300 °C) enhances crystallinity of the active $CsPbI_3$ but dramatically reduces the PL for all composites. The PL spectra of $(CsPbI_3)_{0.40}(a_gZIF\text{-}62)_{0.60}$ is plotted on a log scale against photon energy to elucidate the nature of the trap states for the composites (Figure 2g and Figure S12). PL emissions consist of a primary Gaussian-type peak and can contain tails on the low-energy shoulders usually being associated with the formation of near-edge traps[33]. For the case of $CsPbI_3$ perovskite, the lower-energy Urbach tail is typically associated with disorder at the crystal surface[34,35]. The Urbach tail slopes for composites remained generally unchanged as sintering temperature increased, demonstrating that the defects at the crystal surface can be well passivated even at the early stages of sintering. This is consistent with the fitting of PL spectra with a two-Gaussian function (Figure S13-S14)[36], in which the low energy peaks contributed only a minor to modest part of the overall intensity.

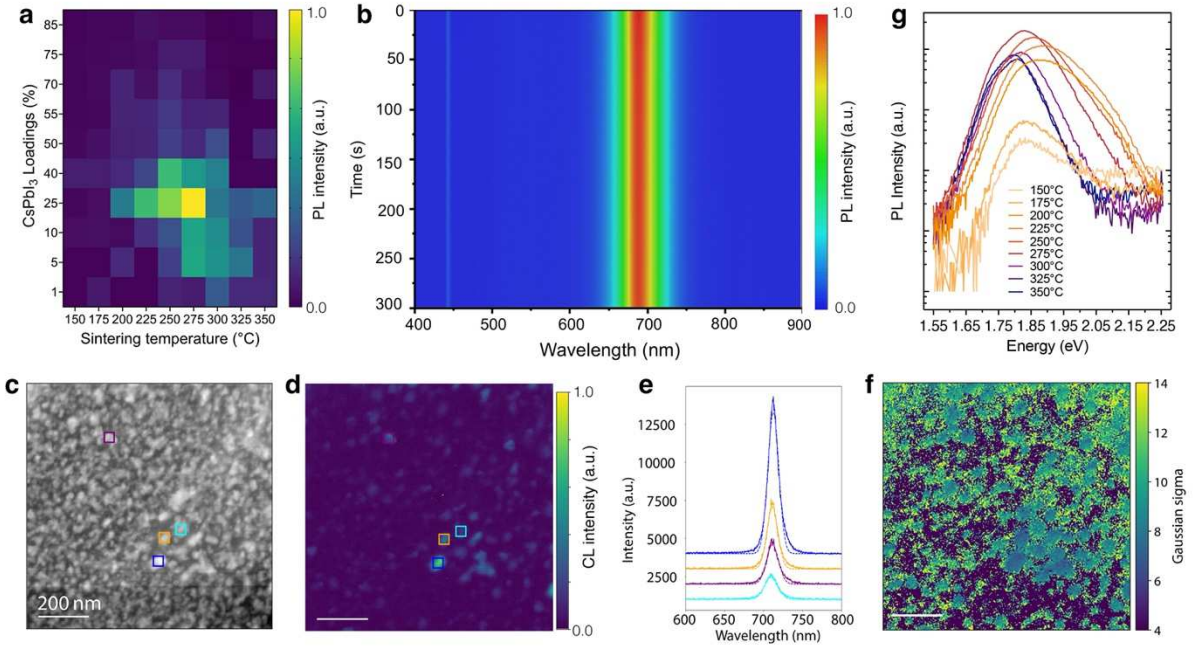

Figure 2. Light emission profile of the composites. (a) Relative PL intensity of different $(CsPbI_3)_X(a_gZIF\text{-}62)_Y$ composites. (b) Evolution of PL spectra under constant laser excitation (440 nm with 82 mW/cm^2) for $(CsPbI_3)_{0.05}(a_gZIF\text{-}62)_{0.95}$. (c) High angle annular dark field (HAADF) image, (d) integrated CL intensity map around the main emission peak at 710 nm and (e) selected CL spectra in the regions of interest marked in E and F. Panel (f) represents the Gaussian fitted σ (nm) values. Scale bar, 200 nm. (g) PL spectra for $(CsPbI_3)_{0.40}(a_gZIF\text{-}62)_{0.60}$ composite shown in log scale.

Composite property evolution during sintering

Differential scanning calorimetry (DSC) can reveal overall information on the thermodynamic and kinetic phase transitions, interfacial interactions and particle aggregations during sintering. DSC curves of pure $CsPbI_3$ and a_gZIF-62 were relatively featureless except for their phase transition (δ- to α-$CsPbI_3$, *ca.* 320 °C) and T_g (a_gZIF-62, *ca.* 290 °C) (Figure S1 and S15). In contrast, a broad endothermal peak for the composites began to develop at temperatures as low as 110 °C (Figure 3a) during the first heating ramp, and the cooling and 2nd heating ramp were featureless, except for the T_g. The endothermal enthalpy of the composite (*ca.* from 110 to 190 °C) was much greater and wider than the phase transition enthalpy of the corresponding $CsPbI_3$. Furthermore, the T_g of the composite decreased with higher $CsPbI_3$ loading, implying that the compositing increased entropy and changed the chemical composition of the a_gZIF-62 phase (Figure 3b and Figure S16).

Particle coarsening and the evolution of a diffusion layer at the interface were identified *via* the synchrotron X-ray small angle scattering (SAXS) on $(CsPbI_3)_{0.1}(a_g\text{ZIF-62})_{0.9}$ composites (Figure 3c and Figure S17). Within the measured scattering vector (q) range, higher temperature sintering coarsened small $CsPbI_3$ particles particularly when temperature approached the T_g (275 °C), where the viscous flow rates of MOF liquid facilitated the diffusion of the perovskite particles. This also suggested the DSC endothermic feature at *ca.* 110 - 190 °C was predominately attributed to phase transition and interfacial interaction, instead of particle coarsening. Further analysis of the SAXS with the Porod's plot (Figure 3d) showed higher sintering temperature led to more significant positive deviation from the Porod's law[37], *i.e.* $\lim q^4 I(q) = K$ when $q \to \infty$, where q is the scattering vector, $I(q)$ is the scattering intensity and K is the Porod constant. The Porod's law describes a system with sharp phase boundary with clear contrast of electron density. The positive deviation may originate in the micro-fluctuations of electron density within the sample, indicating the evolution of a diffusion layer along with sintering.

The development of interfacial bonding within the composites was studied with *in situ* temperature-resolved synchrotron terahertz (THz) FarIR vibrational spectroscopy (Figure S18). The primary characteristics of $(CsPbI_3)(a_g\text{ZIF-62})(10/90)$ can be attributed to Zn-N stretching (*ca.* 300 cm^{-1}) and the aromatic ring deformation (*ca.* 670 cm^{-1}) (Figure S19)[38]. Additional features (*ca.* 135 and 275 cm^{-1}) associated with Zn-I formation emerged from *ca.* 110 °C (concurrent with the endothermal feature in DSC), visible in the 2nd derivative of the *in-situ* spectra (Figure 3e). With further increase of the sintering temperature, the Zn-I features gradually intensified and remained substantially invariant after cooling. Similar behaviour was found in other composite samples (Figure S20-23), and the variation of bonding environment was confirmed by X-ray photoelectron spectroscopy (XPS) (Figure S24-25).

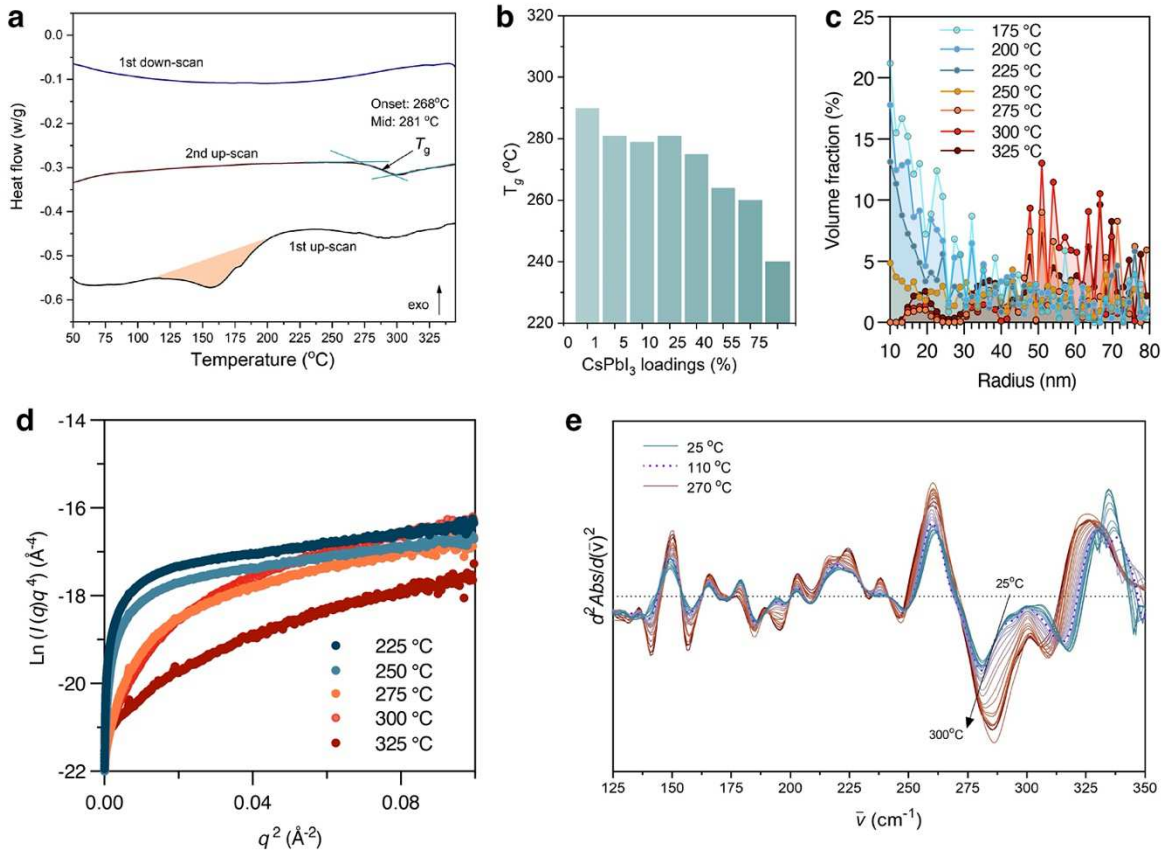

Figure 3. Evolution of interfacial interaction during the sintering. (a) DSC results for $(CsPbI_3)(a_gZIF\text{-}62)(10/90)$. Data was collected under constant flowing nitrogen protection (20 mL/min). The temperature ramping rate for the first up-scan was 20 °C/min, and the ramping rate was 10 °C/min during the DSC cooling and second up-scan. (b) Glass transition temperature, T_g, of the composites as a function of $CsPbI_3$ loading. (c) Particle size evolution for $(CsPbI_3)_{0.1}(a_gZIF\text{-}62)_{0.9}$ composites sintered at different temperature. (d) Change of the Porod's plot of the corresponding SAXS patterns. (e) Second derivative of temperature-resolved *in-situ* THz FarIR spectra for $(CsPbI_3)(a_gZIF\text{-}62)(10/90)$ composites.

Element specific atomic-scale structures at the interface

Solid state nuclear magnetic resonance (SS-NMR) spectroscopy can shed a clear picture on the Cs chemical environment evolution. It identified a nice interplay between different perovskite phases and the greatest proportional contribution of interfacial Cs occurred at 250 °C sintering, correlating with the fluctuation in PL intensity against different sintering temperature. The disordered nature of the glassy matrix was confirmed by the broad ^{1}H and ^{13}C NMR spectra (Figure S26)[39]. In the ^{133}Cs NMR spectra (Figure 4a), for the sample without sintering, the narrow peaks at *ca*. 260 ppm and 280 ppm were attributed to δ-$CsPbI_3$ and CsI, respectively. The broad, low-amplitude signals extending between 0 and *ca*. 350 ppm were attributed to poorly crystalline, highly defective $CsPbI_3$, as expected for mechanochemically synthesised perovskites[23]. After sintering, the broad contributions and CsI peaks diminished, and the major signals stemmed from γ-$CsPbI_3$. Notably, the asymmetric 'shoulder' of the γ-$CsPbI_3$ peaks (below *ca.* 160 ppm, Figure 4a) was related to the γ-$CsPbI_3$ impacted by the chemical environment at the interface, directly in contact with glassy matrix, forming gradient interdiffusion and modified bonding at the interface. Additionally, ^{1}H-^{133}Cs cross-polarization

magic angle spinning (CPMAS) NMR showed a non-negligible cross-polarization transfer between the protons of a_gZIF-62 and the "shoulder-peak" of γ-$CsPbI_3$ at the interface (Figure 4b), pointing to close proximity between the imidazole ligands and Cs atoms. This interfacial Cs contribution was the most substantial for the composite sintered at 250 °C, and gradually decreased along with higher sintering temperature and particle coarsening, showing similar tendency to the variation of PL intensity against different sintering temperatures.

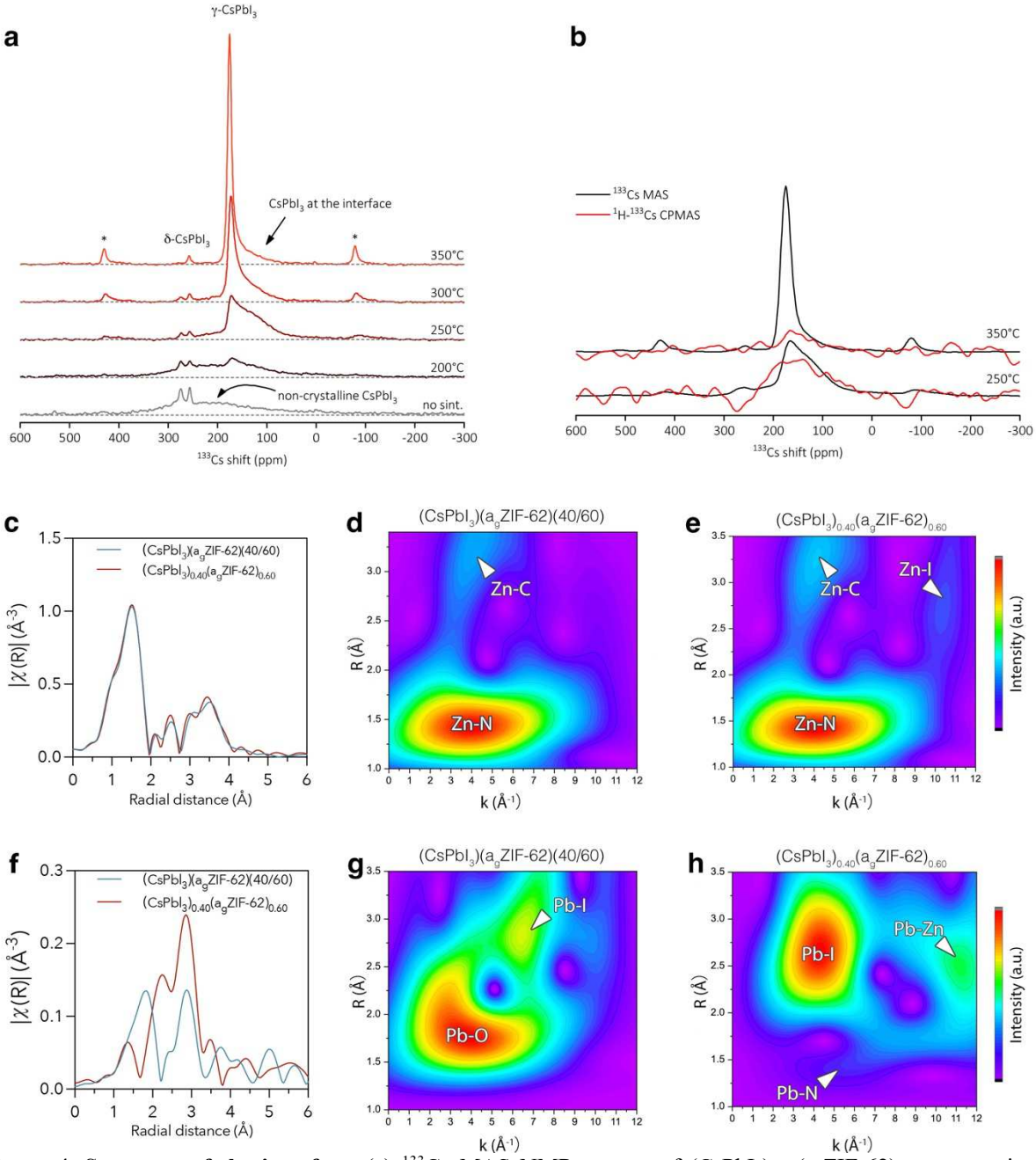

Figure 4. Structure of the interface. (a) ^{133}Cs MAS NMR spectra of $(CsPbI_3)_{0.25}(a_gZIF\text{-}62)_{0.75}$ composites sintered at 200, 250, 300, and 350 °C. (b) ^{1}H-^{133}Cs CPMAS NMR spectra of $(CsPbI_3)_{0.25}(a_gZIF\text{-}62)_{0.75}$ sintered at 250 and 350 °C. (c-e) Extended X-ray absorption fine structure (EXAFS) signal and the full-range wavelet transform (WT) representation for the Zn K edge of $(CsPbI_3)_{0.40}(a_gZIF\text{-}62)_{0.60}$ composites. (f-h) Extended X-ray absorption fine structure (EXAFS) signal and the full-range wavelet transform (WT) representation for the Pb L_3 edge of $(CsPbI_3)_{0.40}(a_gZIF\text{-}62)_{0.60}$ composites. Composites were sintered at 350 °C.

Extended X-ray absorption fine structure (EXAFS) and wavelet transforms (WTs) were performed on to explore the change of Zn and Pb coordination environments through sintering (Figure S27-28), and to identify the change of the first layer structure for these atoms. Wavelet transformation (WT) provides complementary information to FT-EXAFS, which can help differentiate different coordinating pairs at similar atomic distances. EXAFS spectra and wavelet transform contours of the Zn K edge (Figure 4c-e and Figure S28) revealed both samples exhibited main peaks at the R space distance of *ca.* 1.5 Å, corresponding to the distance of Zn-N pairs. The local environment of the Zn prior to sintering was identical in the crystalline ZIF-62[40], indicating Zn atom maintains the tetrahedral configuration within the composites. After sintering, the emerging peak at *ca.* 2.7 Å can be assigned to Zn-I, in good agreement with the THz results. Change to the Pb local environment were more pronounced, particularly considering the evolution of disparate crystal structures (Figure 4f-h and Figure S29). The peaks prior to sintering located at *ca.* 1.7 Å and 2.8 Å can be assigned to Pb-O and Pb-I, respectively[41]. The presence of Pb-O is attributed to the surface oxidation through high energy ball milling synthesis. Crystallisation of $CsPbI_3$ during sintering eliminate the Pb-O bonding and, therefore, Pb-I became more dominating after sintering. In addition, the emerging peak at *ca.* 1.4 Å and 2.5 Å can be attributed to Pb-N and Pb-Zn pairs formed at the interfaces. The formation of new atom pairs was supported by the X-ray adsorption near-edge structure (XANES) of the Pb L_3-edge spectra (Figure S27-28), which exhibit a shift toward lower energy after sintering, due to the higher electronegativity of N and Pb over Zn.

Annular dark-field scanning transmission electron microscopy (ADF-STEM) identified the emergence of interdiffusion alloying layers after high temperature sintering. FIB milling was first used to extract a *ca.* 10 nm thick lamella from a piece of $(CsPbI_3)_{0.1}(a_gZIF\text{-}62)_{0.9}$ sintered at 350 °C to expose individual LHP grains (Figure S30). The sample showed pronounced atomic number contrast between two phases. In STEM, electron energy loss spectroscopy (EELS) provides a sensitive method for analysing the chemical environment using transmitted sub-nanometer electron probes[42]. Although we cannot rule out entirely contributions from FIB milling-induced modifications to the sample, after 350 ℃ sintering, an EELS line scan across the interface quantifies an excess quantity of I outside the $CsPbI_3$ (Figure 5a-b and Figure S31), while such a behaviour was not observed at 275 ℃ sintering (Figure S32). The gradual diffusion of heavier I atoms towards the glassy phase at high temperature aligns with the micro-fluctuation in electron density as demonstrated in SAXS, and the gradual intensified Zn-I THz features up on sintering. The diffusion of Cs, in comparison, has not reached beyond nanometer range from the perovskite grain.

Atomic pair distribution functions (PDFs) identified the interfacial diffusion layers mainly contained Pb-I, Cs-I and Pb-N atomic pairs with only short-range orders. *Ex-situ* synchrotron X-ray total scattering measurements were performed on a series of composites sintered at 350 °C. The PDF, obtained by Fourier transform, showed the short-to-long range fine structure of the composites (Figure 5c). Rietveld analysis of the composite $(CsPbI_3)_{0.50}(a_gZIF\text{-}62)_{0.50}$ was performed with desolvated ZIF-62, γ- and δ-$CsPbI_3$ reference structures. We found that ZIF

structure was only maintained in the short-range order. Good fitting was achieved in the medium and long-range (R_{wp} of 11 % in the range of 15-50 Å), with 13.7 wt% of γ-$CsPbI_3$ and 30.1 wt% of δ-$CsPbI_3$ being identified. The difference pattern in the short-range suggested the structural distortion originated from the surface of the crystalline phases, with the main feature being assigned to Pb-I (*ca.* 3.2 Å). This is an indication of presence of discrete, rigid and slightly distorted Pb-I octahedra within the diffusion alloying layer. These difference features are highly composition- and sintering temperature dependent, showing more contribution from these amorphous perovskite components at higher sintering temperatures, or from composites with larger expected interfaces (Figure S33-34). These observations further confirm the amorphous structures are originated from the interface, instead of the amorphous regions within the bulk perovskites.

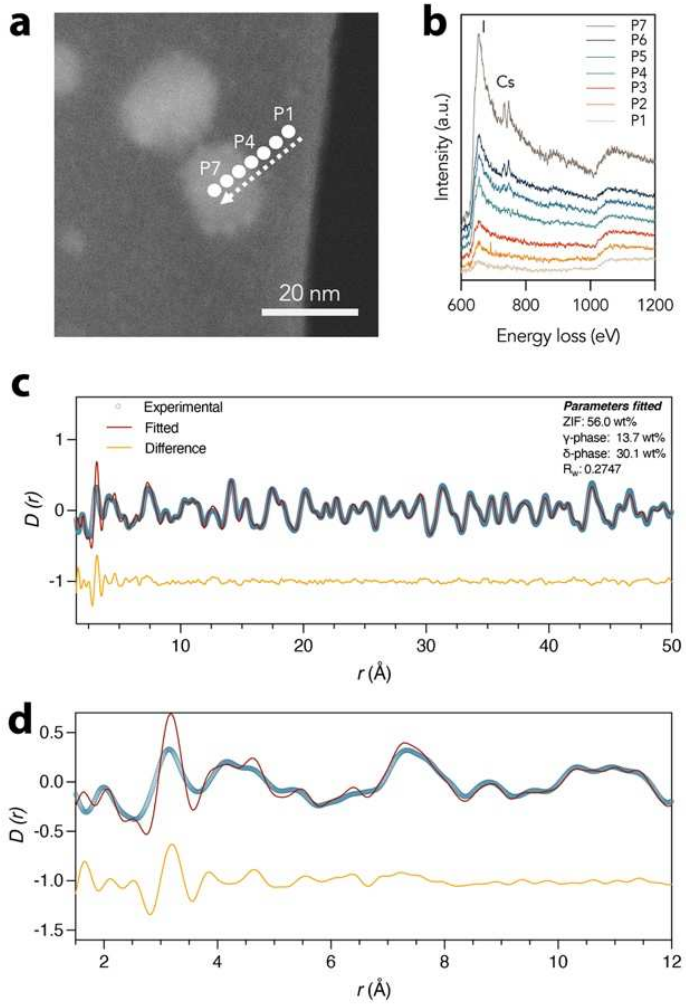

Figure 5. Chemistry and structure of the alloying layer at the interface. (a) ADF-STEM image of $(CsPbI_3)_{0.1}(a_gZIF\text{-}62)_{0.9}$ composites sintered at 350 °C. (b) EELS core loss spectra acquired from the marked points shown in TEM image with background subtracted. (c-d) Atomic pair distribution functions for $(CsPbI_3)_{0.50}(a_gZIF\text{-}62)_{0.50}$ composites sintered at 350 °C. Pair distribution function *D(r)* calculated *via* Fourier transform of the X-ray total scattering function. Panel (d) is the enlarged fitted data in the r range of 1.5-12 Å.

Conclusions and discussions

This study identified the presence of interfacial alloying layers between perovskite and hybrid glass phases, which were mainly consisted of amorphous Pb-I structures. Different behaviours were observed for different atoms during the alloying: high temperature sintering promoted the crystallisation for Cs to form bulk perovskites, possible through a fluxing mechanism. In comparison, the diffusion of the I into the glassy phases was significant (can reach up to *ca.* 10 nm away from the $CsPbI_3$ grain), together with the preservation of Pb-I octahedron structure within the diffused alloying layer.

This work also unveiled the complex performance – property relationship within the perovskite glass composites. We identified that the optoelectronic performance of composite perovskite was predominately determined by the interface, instead of the bulk particle crystallinity. The interfacial alloying favoured the formation of active perovskite phases, stabilised the optoelectronic performance and, more importantly, effectively passivated the trap states. Nevertheless, it can also be detrimental to light emission: for all composites with varying $CsPbI_3$ loadings, the maximum PL intensity was obtained by sintering at a temperature at the corresponding T_g. Above the T_g, glass enters a viscous flowing state, leading to faster diffusion and generate non-stochiometric perovskite near the interface. Though the coarsening can promote the overall crystallinity, the diffusion of Pb-I away from perovskite can lead to non-radiative recombination and quenching of PL.

This study has notable implications for the fundamental understanding of defect formation and control in perovskite materials and the design of halide perovskite devices through interfacial engineering. It exemplified that how the interface can passivate and then generate defects. The investigation of this multimodal system has provided significant progress in comprehending the fundamental processes and interfacial atomic level structures, shedding light onto governing the performance of perovskite materials in practical applications such as solar panels, LEDs and sensing devices. Our findings indicate that prioritising the attainment of bulk crystal perfection may not necessarily lead to the most advantageous outcomes for improving the performance of this particular class of semiconductors. Rather, further research efforts should be focused on interfacial engineering, with consideration of different diffusion behaviour for different perovskite components.

Associated content

Supporting information

Author Information

Corresponding Author

Jingwei.hou@uq.edu.au

Acknowledgments

The authors acknowledge the funding support from the Australian Research Council (ARC) (FT210100589; DP230101901 and FL190100139). We gratefully acknowledge research funding from the Hyogo Science and Technology Association, Japan (Project 4019), and FOCUS Establishing Supercomputing Center of Excellence, Japan. Computational resources were provided by the RIKEN Information Systems Division, Japan (Q22266). This research was supported by an AINSE Ltd. Postgraduate Research Award (PGRA) and Early Career Researcher Grant (ECRG). XL acknowledge the support by an Australian Government Research Training Program (RTP) Scholarship. The authors acknowledge the facilities, and the scientific and technical assistance, of the Australian Microscopy & Microanalysis Research Facility at the Centre for Microscopy and Microanalysis, The University of Queensland. This work used the Queensland node of the NCRIS-enabled Australian National Fabrication Facility (ANFF). This research was undertaken on the THz and SAXS beamline at the Australian Synchrotron, part of ANSTO. SMC acknowledges support from the UK Engineering and Physical Sciences Research Council (EPSRC, EP/V044907/1). This project has been funded in part by the European Union's Horizon 2020 research and innovation programme under Grant Agreements 823717 (ESTEEM3). A.K. and G.M. acknowledge the financial support from the Slovenian Research Agency (research core funding no. P1-0021).

References

1 Das, S., Gholipour, S. & Saliba, M. Perovskites for Laser and Detector Applications. *Energy & Environmental Materials* **2**, 146-153 (2019).

2 Kumawat, N. K., Liu, X. K., Kabra, D. & Gao, F. Blue perovskite light-emitting diodes: progress, challenges and future directions. *Nanoscale* **11**, 2109-2120 (2019).

3 Yoo, J. J. *et al.* Efficient perovskite solar cells via improved carrier management. *Nature* **590**, 587-593 (2021).

4 Zhang, F. *et al.* Metastable Dion-Jacobson 2D structure enables efficient and stable perovskite solar cells. *Science* **375**, 71-76 (2022).

5 Zhang, T. *et al.* Ion-modulated radical doping of spiro-OMeTAD for more efficient and stable perovskite solar cells. *Science* **377**, 495-501 (2022).

6 Steele, J. A. *et al.* Thermal unequilibrium of strained black CsPbI3 thin films. *Science* **365**, 679-684 (2019).

7 Ni, Z. *et al.* Evolution of defects during the degradation of metal halide perovskite solar cells under reverse bias and illumination. *Nature Energy* **7**, 65-73 (2021).
8 Li, X. *et al.* Constructing heterojunctions by surface sulfidation for efficient inverted perovskite solar cells. *Science* **375**, 434-437 (2022).
9 Conings, B. *et al.* Intrinsic Thermal Instability of Methylammonium Lead Trihalide Perovskite. *Advanced Energy Materials* **5** (2015).
10 Chen, Y. *et al.* Dual Passivation of Perovskite and SnO(2) for High-Efficiency MAPbI(3) Perovskite Solar Cells. *Adv Sci (Weinh)* **8**, 2001466 (2021).
11 Tan, S. *et al.* Temperature-Reliable Low-Dimensional Perovskites Passivated Black-Phase CsPbI(3) toward Stable and Efficient Photovoltaics. *Angew Chem Int Ed Engl* **61**, e202201300 (2022).
12 Hou, J. *et al.* Intermarriage of Halide Perovskites and Metal-Organic Framework Crystals. *Angew Chem Int Ed Engl* **59**, 19434-19449 (2020).
13 Shin, J. F. *et al.* Self-assembled dynamic perovskite composite cathodes for intermediate temperature solid oxide fuel cells. *Nature Energy* **2** (2017).
14 Luo, J. *et al.* Halide perovskite composites for photocatalysis: A mini review. *EcoMat* **3** (2021).
15 Xu, X. *et al.* High-Performance Perovskite Composite Electrocatalysts Enabled by Controllable Interface Engineering. *Small* **17**, e2101573 (2021).
16 Han, T. H. *et al.* Perovskite-polymer composite cross-linker approach for highly-stable and efficient perovskite solar cells. *Nat Commun* **10**, 520 (2019).
17 Wang, P. *et al.* Ultrastable Perovskite-Zeolite Composite Enabled by Encapsulation and In Situ Passivation. *Angew Chem Int Ed Engl* **59**, 23100-23106 (2020).
18 Sun, K. *et al.* Three-dimensional direct lithography of stable perovskite nanocrystals in glass. *Science* **375**, 307-310 (2022).
19 Kim, M. *et al.* Conformal quantum dot–SnO2 layers as electron transporters for efficient perovskite solar cells. *Science* **375**, 302-306 (2022).
20 Tan, S. *et al.* Stability-limiting heterointerfaces of perovskite photovoltaics. *Nature* **605**, 268-273 (2022).
21 Zhao, X. *et al.* Accelerated aging of all-inorganic, interface-stabilized perovskite solar cells. *Science* **377**, 307-310 (2022).
22 Hu, J. *et al.* Tracking the evolution of materials and interfaces in perovskite solar cells under an electric field. *Communications Materials* **3** (2022).
23 Hou, J. *et al.* Liquid-phase sintering of lead halide perovskites and metal-organic framework glasses. *Science* **374**, 621-625 (2021).
24 Zheng, Q. *et al.* Understanding Glass through Differential Scanning Calorimetry. *Chem Rev* **119**, 7848-7939 (2019).
25 Marronnier, A. *et al.* Anharmonicity and Disorder in the Black Phases of Cesium Lead Iodide Used for Stable Inorganic Perovskite Solar Cells. *ACS Nano* **12**, 3477-3486 (2018).
26 Abhishek Swarnkar, A. R. M., Erin M. Sanehira, Boris D. Chernomordik, David T. Moore, Jeffrey A. Christians, & Tamoghna Chakrabarti, J. M. L. Quantum dot–induced phase stabilization of α-CsPbI3 perovskite for high-efficiency photovoltaics. *Science* **354**, 95-95 (2016).
27 Shamsi, J., Urban, A. S., Imran, M., De Trizio, L. & Manna, L. Metal Halide Perovskite Nanocrystals: Synthesis, Post-Synthesis Modifications, and Their Optical Properties. *Chem Rev* **119**, 3296-3348 (2019).
28 Guo, R. *et al.* Large-scale continuous preparation of highly stable α-CsPbI3/m-SiO2 nanocomposites by a microfluidics reactor for solid state lighting application. *CrystEngComm* **24**, 3852-3858 (2022).
29 Wei, Y. *et al.* Constructing All-Inorganic Perovskite/Fluoride Nanocomposites for Efficient and Ultra-Stable Perovskite Solar Cells. *Advanced Functional Materials* **31** (2021).

30 Dai, Z., Chen, J. & Yang, B. Yb(2+)-Alloyed Cs(4)PbI(6)-CsPbI(3) Perovskite Nanocomposites for Efficient and Stable Pure-Red Emission. *J Phys Chem Lett* **12**, 10093-10098 (2021).
31 Wang, Y., Chen, Y., Zhang, T., Wang, X. & Zhao, Y. Chemically Stable Black Phase CsPbI3 Inorganic Perovskites for High-Efficiency Photovoltaics. *Adv Mater* **32**, e2001025 (2020).
32 Chu, W., Saidi, W. A., Zhao, J. & Prezhdo, O. V. Soft Lattice and Defect Covalency Rationalize Tolerance of beta-CsPbI3 Perovskite Solar Cells to Native Defects. *Angew Chem Int Ed Engl* **59**, 6435-6441 (2020).
33 Falsini, N. *et al.* Analysis of the Urbach tail in cesium lead halide perovskites. *Journal of Applied Physics* **131** (2022).
34 Chen, Z. *et al.* Cu(2+)-Doped CsPbI(3) Nanocrystals with Enhanced Stability for Light-Emitting Diodes. *J Phys Chem Lett* **12**, 3038-3045 (2021).
35 Zhang, C. *et al.* Unraveling Urbach Tail Effects in High-Performance Organic Photovoltaics: Dynamic vs Static Disorder. *ACS Energy Letters* **7**, 1971-1979 (2022).
36 Wen, X., Yu, P., Toh, Y.-R., Hao, X. & Tang, J. Intrinsic and Extrinsic Fluorescence in Carbon Nanodots: Ultrafast Time-Resolved Fluorescence and Carrier Dynamics. *Advanced Optical Materials* **1**, 173-178 (2013).
37 Koberstein, J. T., Morra, B. & Stein, R. S. The determination of diffuse-boundary thicknesses of polymers by small-angle X-ray scattering. *Journal of Applied Crystallography* **13**, 34-45 (1980).
38 Hou, J. *et al.* Halogenated Metal-Organic Framework Glasses and Liquids. *J. Am. Chem. Soc.* **142**, 3880-3890 (2020).
39 Baxter, E. F. *et al.* Combined experimental and computational NMR study of crystalline and amorphous zeolitic imidazolate frameworks. *Phys. Chem. Chem. Phys.* **17**, 25191-25196 (2015).
40 Bennett, T. D. *et al.* Melt-Quenched Glasses of Metal-Organic Frameworks. *J Am Chem Soc* **138**, 3484-3492 (2016).
41 Ye, T. *et al.* Below 200° C fabrication strategy of black-phase CsPbI3 film for ambient-air-stable solar cells. *Solar RRL* **4**, 2000014 (2020).
42 Collins, S. M. *et al.* Functional Group Mapping by Electron Beam Vibrational Spectroscopy from Nanoscale Volumes. *Nano Lett* **20**, 1272-1279 (2020).